Measurement Science and Technology

PAPER • **OPEN ACCESS**

A spatially resolved *in situ* calibration applied to infrared thermography

To cite this article: Maximilian Elfner *et al* 2019 *Meas. Sci. Technol.* **30** 085201

OPEN ACCESS
IOP Publishing
Measurement Science and Technology
Meas. Sci. Technol. **30** (2019) 085201 (9pp)
https://doi.org/10.1088/1361-6501/ab1db5

A spatially resolved *in situ* calibration applied to infrared thermography

Maximilian Elfner, Tobias Glasenapp, Achmed Schulz and Hans-Jörg Bauer

Institute of Thermal Turbomachinery (ITS), Karlsruhe Institute of Technology (KIT), Kaiserstrasse 12, Karlsruhe, Germany

E-mail: maximilian.elfner@kit.edu

Received 11 February 2019, revised 15 April 2019
Accepted for publication 29 April 2019
Published 28 June 2019

Abstract

When using thermography at elevated ambient temperature levels to determine the surface temperature of test specimen, radiation reflected on the test surfaces can lead to a large measurement error. Calibration methods accounting for this amount of radiation are available in the open literature. Those methods, however, only account for a scalar calibration parameter. With new, complex test rigs and inhomogeneous reflected radiation distribution, the need for a spatially resolved calibration arises. Therefore, this paper presents a new correction method accounting for a spatially varying reflected radiation. By computing a geometrical ray-tracing, a spatially resolved correction factor is determined. An extended calibration technique based on an *in situ* approach is proposed, allowing a local correction of reflected radiation. This method is applied to a test case with defined boundary conditions. The results are compared to a well-known *in situ* calibration method. A major improvement in measurement accuracy is achieved: the error in calibrated temperature can be reduced from over 10% to well below 2.5%. This reduction in error is especially prominent when the test surfaces are colder than the hot ambient, which is the case in many cooling applications, e.g. in gas turbine cooling research.

Keywords: thermography, calibration, ray tracing, offset radiation

Nomenclature

Latin

C	(A.U.)	Corrector
E	(A.U.)	Incident irradiation
I	(A.U.)	Scaled, linearized detector signal
T	(K)	Temperature
U	(A.U.)	Detector signal
W	(W (m^2 µm))	Specific spectral irradiation
$\vec{X}$	(m)	Location
c	(m s^{-1})	Speed of light
h	(J s^{-1})	Planck constant
h	(W (m K)$^{-1}$)	Heat transfer coefficient
k	(J K^{-1})	Boltzmann constant
l	(m)	Length
$\{r, b, f\}$	(A.U.)	Calibration constants

Greek

Γ	(−)	Temperature ratio
Δ	(−)	Distance
Ξ	(−)	Radiation ratio
ϵ	(−)	Emissivity ratio
ε	(−)	Emissivity
ϑ	(rad)	Azimuth angle
θ	(°)	Angle of view
λ	(µm)	Wavelength
ϱ	(−)	Reflectivity
τ	(−)	Transmissivity
φ	(rad)	Polar angle

Scripts

∞	Free stream
C	Combined

D	Detector
S	Surface
W	Wall
a	Ambient
bb	Blackbody
c	Corrected, equation (10)
co	Coolant
lat	Laterally averaged
nc	Not corrected, equation (5)
off	Offset
tot	total
ts	Test surface
wi	Window
x	Running length

Abbreviations

LSQ	Least squares
Nu	Nusselt number
Re	Reynolds number

1. Introduction

Infrared thermography is used in a multitude of applications to determine high resolution surface temperature maps. At the current time, it is the most capable tool for resolving surface temperatures with high accuracy at high temperatures. The main alternative, thermo-sensitive paint, can reach equal levels of accuracy [1–3], however the application temperature is limited. Thus, especially in gas turbine cooling research with high temperatures present, infrared thermography is a well known and often used method [4–7]. However, the measurement system is a radiation detector only. Thus, extensive calibration has to be performed to derive temperatures with low residual measurement error from the radiation information. The effort for this calibration increases with the complexity of the radiation situation. Based on several new calibration techniques developed at the Institute of Thermal Turbomachinery (ITS) in the recent past, a new corrector will be presented. This new correction factor enables low error thermography in enclosed, hot, test setups with limited optical access. The aim of this paper is to derive and validate this new calibration technique and show its applicability to thermography measurements.

Perfectly radiating surfaces at temperatures above 0 K emit radiance of a certain specific spectral intensity W_{bb} following Planck's law with

$$W_{\mathrm{bb}}(\lambda, T_{\mathrm{S}}) = \frac{2\pi hc^2}{\lambda^5 (\mathrm{e}^{\frac{hc}{\lambda k T_{\mathrm{S}}}} - 1)}, \tag{1}$$

where λ, h, c, k are the wavelength of the emitted radiance, the Planck constant, the Speed of Light and the Boltzmann constant. With non-ideal surfaces, the radiance W_{S} is generally lower. For those surfaces, this reduction in emitted radiance is characterized by the emissivity of the surface ε_{S}.

$$W_{\mathrm{S}}(\lambda, \theta, T_{\mathrm{S}}) = \varepsilon_{\mathrm{S}}(\lambda, \theta, T_{\mathrm{S}}) \cdot W_{\mathrm{bb}}(\lambda, T_{\mathrm{S}}), \tag{2}$$

which itself is a function of wavelength, temperature and angle of view θ. To achieve a well defined radiation signal, the test surfaces are commonly coated with special high emissivity coatings, which exist for a wide range of application temperatures [8, 9]. Those coatings have two main benefits: a high emissivity in the range of $\varepsilon \geqslant 0.95$ and a mainly diffuse reflective characteristic [10]. The high emissivity, and thus low reflectivity, yields an advantageous signal-to-offset ratio, while the diffuse reflectivity acts as a spatial low-pass filter for the structures reflected on the coated surface, thus damping their spatial gradients. For narrow-band infrared detectors and comparably flat surfaces, a gray body estimation with $\varepsilon_{\mathrm{S}} = \text{const.}$ is valid. If the emissivity is unknown or differs from the gray body estimation, multiple wavelengths may be used [11, 12]. However, a final calibration has to be performed in this case too ([11] chooses the method used here and developed by [12, 13], chooses a polynomial approach). The measurement effort increases drastically due to the need of two camera systems or complex filter designs.

The radiance emitted by the test surface passes several optical obstacles (e.g. windows, atmospheres, the camera lens), which all reduce the radiation intensity. This reduction is defined by the product of each of the obstacles' transmissivities $\tau_{\mathrm{tot}} = \prod_i \tau_i$. Additionally, radiation emitted from other enclosing surfaces is reflected by the test surface towards the detector. This radiance is termed offset radiance E_{off} and adds to the surface's radiance signal. The radiance emitted by the highly translucent parts in the optical path is comparably small and not explicitly separated in the calibration. However, when using an *in situ* approach, it will be accounted for. Thus, the radiance signal at the infrared detector E_{D} is

$$\begin{aligned} E_{\mathrm{D}}(\lambda, T_{\mathrm{S}}, T_i) &\propto \tau_{\mathrm{tot}}(\lambda, T_i) \cdot \left(W_{\mathrm{S}}(T_{\mathrm{S}}) + W_{\mathrm{off}}(T_i)\right) \\ &\propto E_{\mathrm{S}} + E_{\mathrm{off}}. \end{aligned} \tag{3}$$

To relate this radiance level to a physical surface temperature, Martiny *et al* [14] proposed a semi-empirical calibration function for the detector signal U_{D}, which is derived from inverting equation (1):

$$T_{\mathrm{S}}(\vec{X}) = \frac{b}{\ln(\frac{r}{U_{\mathrm{D}}(\vec{X})} + f)}. \tag{4}$$

The three free parameters $\{r, b, f\}$ then need to be determined individually for each experiment. Schulz [15] shows the validity of an *in situ* calibration method which can be applied to either closed or open measurement setups. This calibration technique is especially feasible with high ambient temperatures. Other methods rely on modeling the radiation flux [2] but still require a final *in situ* calibration. At lower temperatures, different calibration functions were proposed [4, 6, 16, 17]. While using different approaches on modeling the radiation situation, they all rely on a final *in situ* calibration. Thus, each infrared image needs to include calibration points with known radiance-temperature-relation (the number depending on the calibration parameters, three in the case of equation (4)). This is commonly achieved by implementing small-scale thermocouples in the test surface.

Depending on size, complexity and boundary conditions of the test surface, including several thermocouples can be challenging. Also, reducing the calibration error by using a

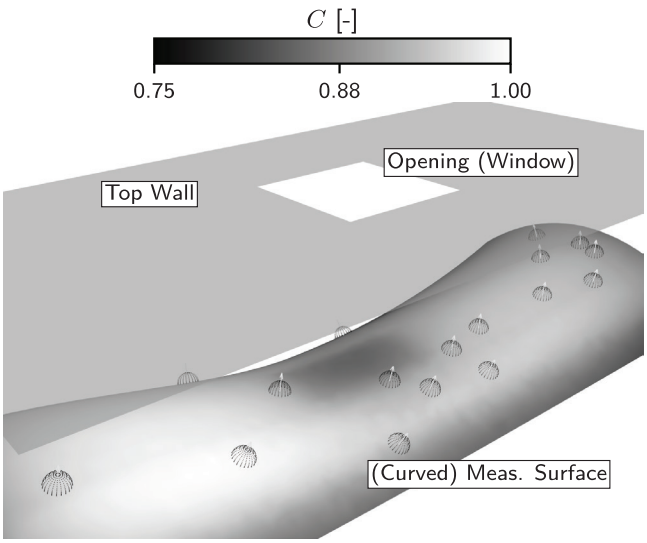

Figure 1. Example of spatially varying offset radiance, represented with a Corrector $C[-] \in [0, 1]$. The top plate shows a small opening e.g. for a window.

least-squares (LSQ) fit is beneficial. Thus, a reduction of free parameters of the calibration function equation (4) is desirable. Ochs *et al* [13, 18] present several methods which, in conjunction, allow the calibration of thermography measurements with only one free parameter in the calibration function. First, they explicitly separate the specific irradiance of the test surface and the offset radiance in the calibration function by combining equations (3) and (4). Ochs *et al* [13] show that this is only valid with a scaled and linearized detector signal $I_D = I_S + I_{off} \propto E_D$.

$$T_S(\vec{X}) = \frac{b}{\ln(\frac{r}{I_D(\vec{X}) - I_{off}} + f)}. \tag{5}$$

Next, they show that in most technical cases a pre-calibration can be performed in a simple setup, allowing the determination of $\{r, b, f\}$ in advance. Thus, only the offset radiance needs to be determined with an *in situ* method. This offset radiance is mainly influenced by surroundings with high temperatures compared to the test surface, which is of main importance for e.g. cooled components in hot environments. In the final *in situ* calibration, the offset radiance I_{off} is then determined as a scalar calibration parameter.

However, new experimental data suggests that the assumption of scalar offset radiance I_{off} is not always justified. Thus, during the following sections a new method will be presented and validated, allowing the correction of locally varying offset radiance.

2. Effects of non-Homogeneous offset radiance

In certain measurement setups, the offset radiance can not be assumed as a constant value. With only diffuse reflectivity, a point on a surface will reflect all incoming radiation from its full hemisphere towards the detector. If there is a change in offset radiance (e.g. a small window in the opposing wall), this structure will imprint on the test surface, leading to locally changing offset radiances. Figure 1 shows such a situation: a scalar representation

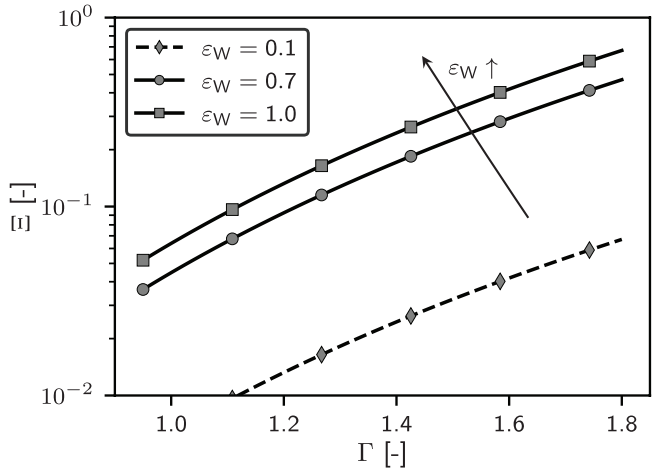

Figure 2. Ratio of offset irradiance to object irradiance Ξ at different temperature ratios Γ for common wall emissivities ε_W computed using a simplified approach.

of the offset radiance was computed for qualitative display, clearly showing the localized effect of the small opening in the top wall. In this case, using a point-based *in situ* calibration method with constant offset radiance leads to a change in measured surface temperature only due to a change in this radiance.

This measurement error greatly depends on the ratio of surface to offset radiation $\Xi = \frac{W_{off}}{W_S} \approx \frac{E_{off}}{E_S}$. A first estimation of this uncertainty can be performed by assuming a $\propto T^4$ relation for the radiation power (Stefan–Boltzmann law[1]) and different ratios of temperature $\Gamma = \frac{T_W}{T_S}$ and emissivity $\epsilon = \frac{\varepsilon_W}{\varepsilon_S}$ at an exemplary nominal test surface temperature of $T_S = 350$ K and an emissivity of $\varepsilon_S = 0.95$. The results of this estimation are shown in figure 2. With increasing temperature ratio Γ, the amount of offset radiance quickly approaches same orders of magnitude as the object radiance, leading to a large influence on measurement uncertainty. A decrease in wall emissivity can improve (lower) the radiation ratio Ξ. An exemplary value of $\varepsilon_W = 0.1$ for a e.g. mirrored surface is shown in figure 2, however this is technically difficult to achieve. Thus, a typical value for oxidized steel is plotted as reference ($\varepsilon_W = 0.7$, stainless steel, oxidized at elevated temperatures [22]). Even at lower temperature ratios, the amount of offset radiance is high and needs to be corrected. It is worth noting that when working in open setups, the ambient emissivity approaches one. This curve is also shown in figure 2 ($\varepsilon_W = 1$). Even at temperature ratios close to unity, the effect of the ambient radiation needs to be considered, making an *in situ* calibration mandatory not only in closed channel setups, but also for high accuracy thermography in open setups.

To include changing offset radiance in the calibration procedure, this radiation has to be determined as a function of object space $E_{off} = f(\vec{X})$. To avoid complex ray-tracing based on radiation power with several assumptions on surface and atmospheric properties, the presented approach is divided into two steps. First, a correction field $C = f(\vec{X})$ of arbitrary unit is

[1] Which is only valid for the full spectrum of radiation—when calibrating the actual camera system later on, an equation considering the spectral band of the detector is used [19–21].

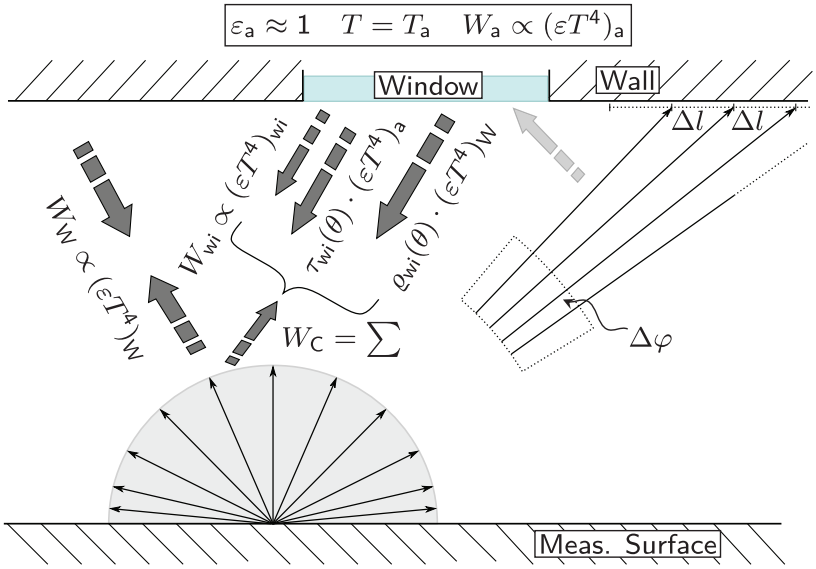

Figure 3. Quantities used during the computation of the corrector on the measurement surface. Typically, one or more windows exist which have different radiation properties than the surrounding walls.

computed from the geometry and only few assumptions. This field represents a relative magnitude of the offset radiance and thus can be scaled to $C \in (0, 1]$. In a second step, this correction field is implemented into the *in situ* calibration process, yielding a corrected temperature field.

3. Computation of a spatially resolved corrector

The computation of the corrector presented in this study is based on a simplified geometrical ray-tracing approach. The aim of the algorithm is to produce a locally resolved corrector map $C = f(\vec{X})$ which represents the radiation situation in arbitrary units. Only few input quantities are necessary: the test surface geometry, the geometry of the surrounding surfaces, and emissivities and surface temperatures of those surfaces. Since only relative values are determined and later calibrated to physical quantities, the method is robust in terms of an error in estimated emissivities or temperatures.

As a first step, the test surface is discretized and a radiation hemisphere is built at each point. The resolution of the surface discretization is chosen to approximately match the camera system's resolution. The discretization in the spherical coordinates φ, ϑ of the hemisphere has to be chosen considering the geometry of the surrounding surfaces. A projected surface element needs to be able to resolve the smallest structure of the geometry. This is shown in figure 3 for a 2D case, where the projected surface reduces to the projected length Δl. Additionally, the polar discretization needs to be of non-uniform spacing. For two opposing surfaces, the projected line element can be computed as

$$\begin{aligned} \mathrm{d}l &= \mathrm{d}\big(h \cdot \sin(\varphi)\big) \\ &\propto \mathrm{d}\varphi \cdot \cos(\varphi) \end{aligned} \tag{6}$$

and thus, for a homogeneous distribution of Δl:

$$\Delta\varphi \propto \big(\cos(\varphi)\big)^{-1}. \tag{7}$$

The resulting radiation hemisphere in 3D is exemplarily shown in figure 4. The default hemisphere is copied to each surface point (gray center) and oriented along the local surface normal (black arrow). Thus, at each test surface point, $N_\varphi \times N_\vartheta$ rays can be formed by joining the center and each point on the hemisphere.

Following, the ray-triangle intersection problem for all rays from step one and all triangles from the surrounding geometry discretization is solved. Only first order rays are considered. For large problem sizes, Plücker space is recommended to speed up computation [23, 24]. Two main cases have to be differentiated (both depicted in figure 3):

- Ray i intersects with a solid wall element triangle k. By only considering first order rays, a value of $C_i = (\varepsilon T^4)_W$ is assigned to the ray.
- Ray i intersects with a window element triangle j. Since the optical properties of translucent materials show a strong dependency on angle of view θ_{ij}, this angle has to be computed using the (Eulerian) vector representation of the ray $\vec{r}_i$ and the local normal of the intersected triangle $\vec{n}_j$:

$$\cos(\theta_{ij}) = \frac{\vec{r}_i \cdot \vec{n}_j}{\|\vec{r}_i\|_2 \cdot \|\vec{n}_j\|_2}. \tag{8}$$

Two of the three window material's parameters emissivity $\varepsilon \neq f(\theta)$, reflectivity $\varrho = f(\theta)$ and transmissivity $\tau = f(\theta)$ have to be determined from material functions, the third follows from Kirchhoff's law with $\varepsilon + \varrho + \tau = 1$. In most technical setups, those properties are independent of the window's temperature T_{wi}. For sapphire, which is commonly used as a window material, those parameters are supplied by Thomas *et al* [25] and Fowles [26], pp 45.

The resulting correction factor can be computed as the sum of the three contributing irradiances and the assump-

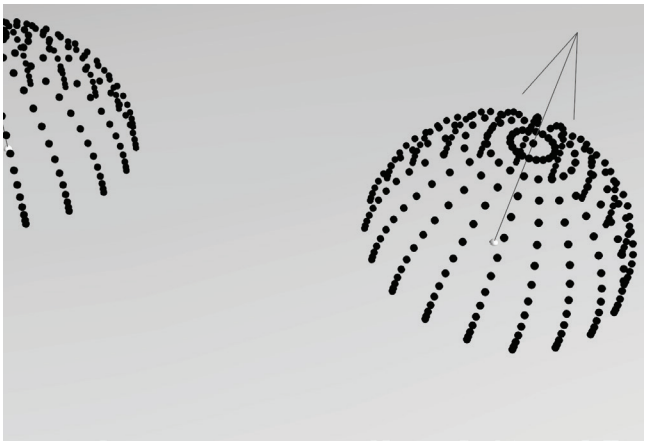

Figure 4. 3D representation of the radiation hemisphere discretization on the measurement surface. The distance of each point reduces in polar direction when approaching the surface.

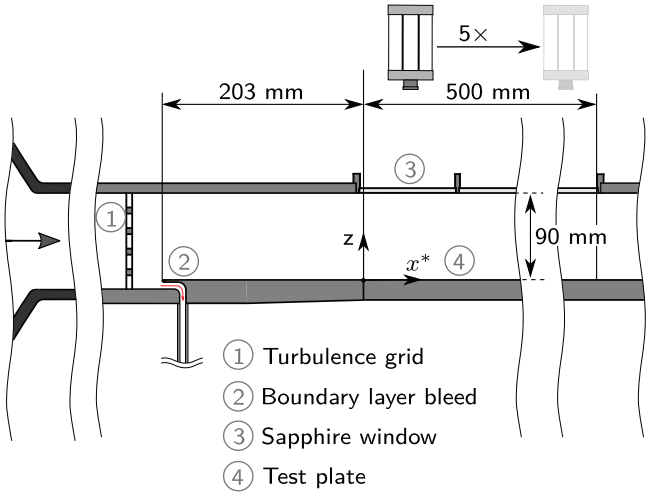

Figure 5. Cross-sectional view of the test section (adapted with permission from [27]). Flow direction from left to right. Camera position shown above test rig.

tion that reflections in the window show the high radiance of the wall:

$$C_i = \varrho_{ij} \cdot (\varepsilon T^4)_\mathrm{W} + \tau_{ij} \cdot (\varepsilon T^4)_\mathrm{a} + (\varepsilon T^4)_\mathrm{wi}. \tag{9}$$

Finally, the mean value of all ray-specific correction factors C_i is computed at each test surface point. With the spatially adapted discretization presented before, an arithmetic mean can be performed, yielding a scalar field of correction factors $C = f(\vec{X})$.

4. Extended *in situ* calibration technique

The determined corrector has to be included into the calibration procedure. With $C \in (0, 1]$ and $C = 1$ describing the maximum offset radiance for a given setup, the calibration equation (5) is extended to include C:

$$T_\mathrm{S}(\vec{X}) = \frac{b}{\ln\left(\frac{r}{I_\mathrm{D}(\vec{X}) - C(\vec{X}) \cdot I_\mathrm{off}} + f\right)}. \tag{10}$$

Table 1. Boundary Conditions and assumptions for the test case.

Test conditions	
Freestream temperature	$T_\infty = 510$ K
Radiative properties: walls	
Emissivity	$\varepsilon_\mathrm{W} = 0.7$
Temperature	$T_\mathrm{W} = 480$ K
Radiative properties: windows	
Emissivity	$\varepsilon_\mathrm{wi} = 0.04$
Transmissivity	$\tau_\mathrm{wi} = f(\theta)$
Reflectivity	$\varrho_\mathrm{wi} = f(\theta)$
Temperature	$T_\mathrm{wi} = 480$ K
Radiative properties: ambient	
Emissivity	$\varepsilon_\mathrm{a} = 1$
Temperature	$T_\mathrm{a} = 300$ K

With knowledge of C at the *in situ* calibration point locations, this equation can again be solved with the same methods as equation (5), since I_off remains as the only free, scalar parameter. Thus, still only one calibration point is required, whereas more can be used for a LSQ method. The resulting scalar offset radiance I_off represents the maximum value of a given setup.

5. Application to heat transfer measurements

The presented calibration procedure is applied to experimentally acquired data. First, the test rig will be presented. This setup is suitable for verification since the boundary conditions and the expected results are well known. Second, the effect of the new correction method on the heat transfer results will be evaluated.

5.1. Test case

A test rig for the investigation of heat transfer on a flat plate is used to validate the correction procedure. The rig is schematically shown in figure 5 and presented in detail in [27]. The boundary conditions and assumed radiative properties are presented in table 1.

Well conditioned, homogeneous flow enters the closed, rectangular channel (500 mm · 90 mm) from the left at elevated temperatures T_∞. The main measurement section consists of a back-cooled, flat plate with a boundary layer removal and a turbulence grid just upstream. The turbulence intensity at the beginning of the measurement plate is $Tu \approx 8.5\%$. The test plate is water-cooled and the parts upstream of the test plate can be considered nearly adiabatic. Thus, there is a sudden change in thermal boundary conditions. In the lateral direction, only the mid-section (80 mm) of the plate is investigated, thus no lateral temperature gradients are present. Following the test surface downstream, a constant increase in boundary layer thickness and thus a constant decrease in heat transfer coefficient h_S and surface temperature T_S is expected.

For both test cases, the sapphire window mounted in the top plate is deliberately placed out of center (window centerline moved laterally to higher y). Additionally, both the window's upstream edge and downstream edge are close to the

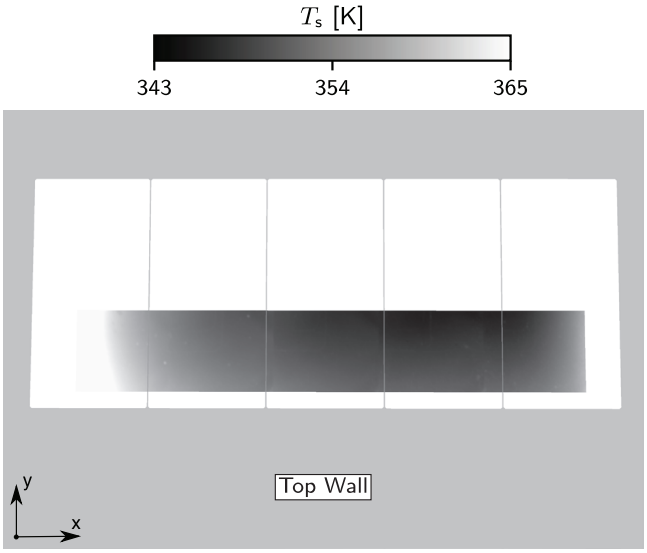

Figure 6. Calibrated surface temperature T_S looking through the top window using the basic approach equation (5). A non-physical, asymmetrical reduction in calibrated temperature is visible below the windows in y^+-direction due to the reduction in reflected radiation below the large opening.

perimeter of the investigated area. This generates an asymmetrical distribution of offset radiance in lateral and streamwise direction.

The infrared system (FLIR SC6000 with a 50 mm lens and 4.1 µm cut-off filter, resulting a spectral sensitivity of 3 . . . 4.1 µm) is mounted above the test rig looking downward and is moved downstream, recording five overlapping positions in streamwise direction. At each position, images are recorded at 30 Hz for a single second using a 0.5 ms integration time per image and, subsequently, time-averaged. The resulting image is pre-calibrated applying a detector linearization and a non-uniformity correction [13]. The resulting images are stitched together using the mean value at overlapping areas and calibrated with *in situ* thermocouples implemented in the test plate. This final temperature calibration is performed with the earlier technique equation (5) (subscript $\square_{nc}$) and the new technique equation (10) (subscript $\square_c$).

The result of the calibration procedure without correction is shown in figure 6. Looking through the top window on the test surface, the calibrated temperature evaluated at the center of the test surface is shown. A lateral asymmetric decrease in surface temperature is visible in y^+-direction, especially at the center of the window in streamwise, x^+-direction. In this area, the radiation reflected on the test surface is low. When calibrating globally, this decrease in reflected radiation and thus decrease in radiation recorded by the detector leads to an (unphysical) decrease in recorded surface temperature.

5.2. Verification

Figure 7 shows the normalized, laterally averaged temperature T^*_{lat} along the surface length of the measurement plate x^*. The temperature is normalized using the maximum temperature of the case without the corrector. Due to the change in thermal

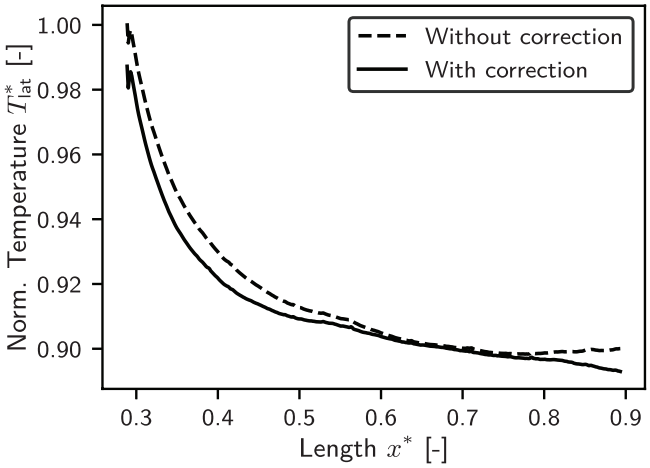

Figure 7. Normalized, laterally averaged temperature T^*_{lat} over normalized running length x^* with and without the proposed corrector.

boundary condition, the temperature decreases with surface length. In the downstream region, an increase of temperature can be observed for the non corrected approach. This is a measurement error due to the fact that the offset radiance increases with the end of the top window. For the case with the corrector, the normalized temperature is below the one for the case without the corrector. Especially near the upstream and downstream end of the test plate, this becomes evident. Between $x^* = 0.6 \ldots 0.8$, there is nearly no effect of the corrector: the calibration of the non-corrected approach was performed mainly in this area and thus represents this value of offset radiance quite well.

In order to further verify the correction, measurement data is now shown as lat. avg. Nusselt numbers $\mathrm{Nu}_{x,lat}$[2] and compared to a correlation by Reynolds [28]. This is shown in figure 8 with the surface length Reynolds number Re_x on the x-axis. The correlation shows the peak in Nusselt number at the upstream end of the test plate. This is due to the change of thermal boundary condition and the related boundary layer change. Nusselt numbers increase with increasing surface length Reynolds number. Measurement data with and without the corrector is qualitatively in good agreement with the correlation. At the end of the measurement plate, Nusselt numbers calculated from the measured temperatures increase. This is due to a change in thermal boundary condition at the very end of the test plate. Data is not evaluated in this region. A quantitative comparison of both data sets shows that Nusselt numbers based on the temperature measurements without correction are higher than the values of the correlation. The data based on the corrected temperature is in excellent agreement with the correlation and effects of the sapphire windows near the upstream and downstream end of the test plate thus are corrected.

The positive effect of the corrector is even more drastic in the lateral direction. Figure 9 shows the normalized

[2] Nusselt numbers are derived from finite element heat flux calculations with the measured temperature field on the test surface as boundary condition. The hot gas recovery temperature is chosen as reference for the heat transfer coefficient.

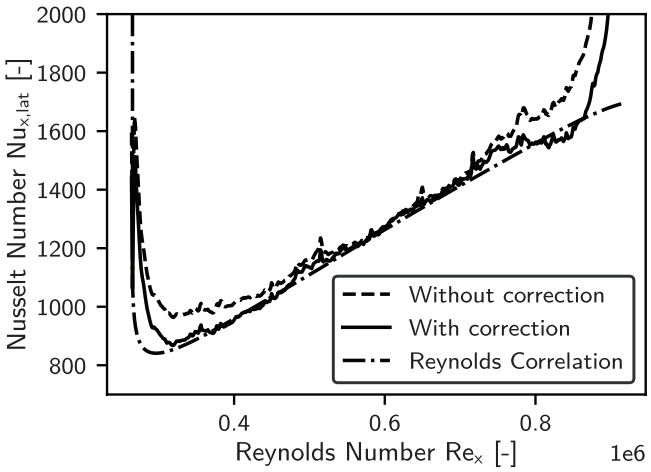

Figure 8. Laterally averaged Nusselt Numbers $Nu_{x,lat}$ over running length Reynolds number Re_x with and without the proposed corrector. Additionally, a Reynolds correlation is shown.

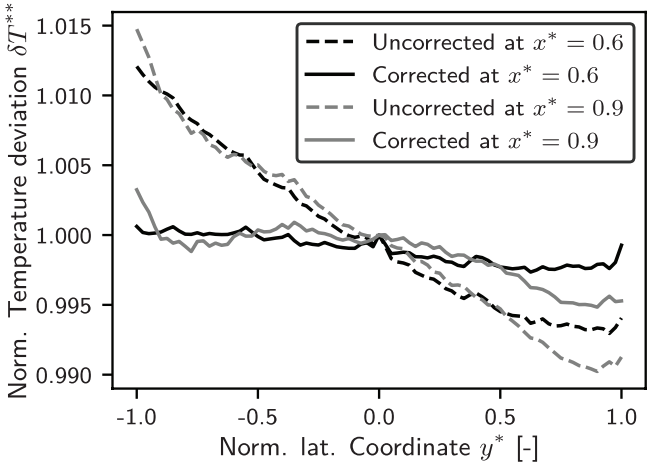

Figure 9. Normalized deviation in the lateral temperature distribution δT^{**} at different values in the streamwise direction x^*.

temperature deviation in the lateral direction $\delta T^{**} = \frac{T}{T|_{y^*=0}}$ against the normalized lateral coordinate y^* at different positions in streamwise direction. The test case suggests a uniform temperature distribution in the lateral direction. It is evident that temperature measurements without correction show a non-uniformity in lateral direction. Temperatures tend to increase with the negative $y*$-direction. This is not a physical effect, but a measurement error due to the increase in offset radiance I_{off}. The error is strongly reduced when the correction method presented in this study is used.

Finally, the surface temperature field is evaluated. Figure 10 shows this field in the same manner as figure 6, however now using the proposed calibration procedure with locally resolved offset radiance. The corrected temperature field now is symmetric in lateral direction—the effect of asymmetrical offset radiance is removed. The decrease in temperature due to the change in boundary layer thickness is clearly visible.

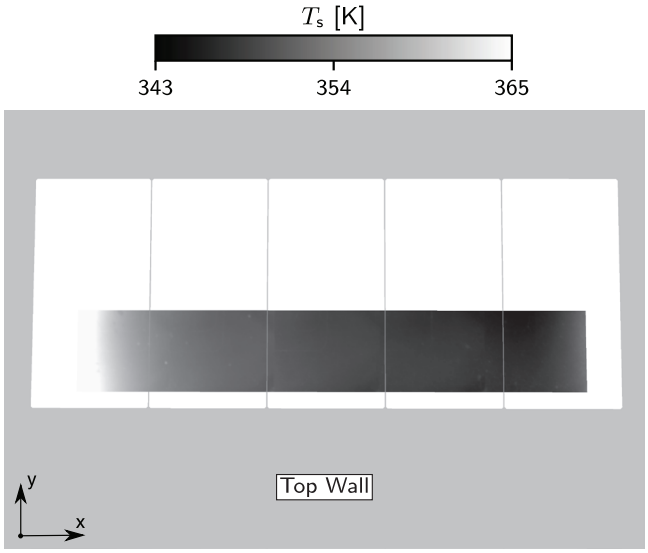

Figure 10. Calibrated surface temperature T_S looking through the top window using the proposed approach equation (10). The non-physical, asymmetrical reduction in calibrated temperature is almost completely removed. The physical temperature decrease in streamwise direction is preserved.

6. Linear error estimation

Finally, the increase in measurement accuracy and the residual error will be evaluated. Linear error propagation has been computed for the full data evaluation chain with and without the corrector.

Differentiating the calibration equation (10) yields the relative error ΔT_i^* at a certain nominal surface temperature T_i:

$$\Delta T = \frac{\partial T}{\partial I_{\text{D}}} \cdot \Delta I_{\text{D}} + \frac{\partial T}{\partial I_{\text{off}}} \cdot \Delta I_{\text{off}} + \frac{\partial T}{\partial C} \cdot \Delta C, \quad (11a)$$

$$\Delta T_i^* = \frac{\Delta T_i + \Delta T_{\text{const.}}}{T_i}. \quad (11b)$$

With the uncertainties in acquired or calibrated quantities: the detector uncertainty ΔI_{D}, the offset radiation uncertainty ΔI_{off} and the uncertainty of the new corrector ΔC. The same pre-calibration is performed for both cases and thus, the uncertainty in r, b, f is omitted in this calculation. The values for the uncertainties are given in equation (12). The radiation uncertainties are derived from the experience at the ITS and the documentation available [13, 29–31]. The uncertainty for the corrector is either the estimated range for a given computation if the correction is not applied (subscript $_{\text{nC}}$) or the residual uncertainty which was estimated from multiple computations with different parameters for emissivities and temperatures of the important parts if the correction is applied (subscript $_{\text{C}}$).

$$\Delta I_{\text{D}} = 0.5\%, \quad (12a)$$

$$\Delta I_{\text{off}} = 5\%, \quad (12b)$$

$$\Delta C_{\text{nC}} = 0.4, \quad (12c)$$

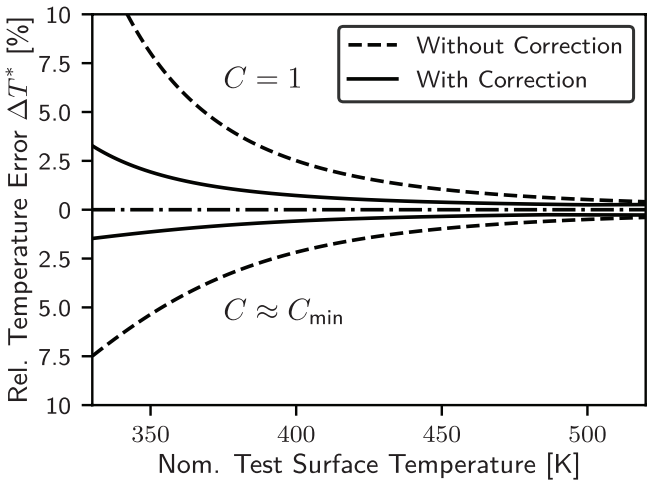

Figure 11. Measurement uncertainty defined as relative temperature error ΔT^* over a common range of measurement surface temperatures computed using a linear error propagation method for the case with and the case without the proposed corrector. The upper half shows the error for maximum offset radiation $C = 1$, the lower half shows the error for a comparably low offset radiation $C_{\min}$.

$$\Delta C_C = 0.04. \tag{12d}$$

The determined uncertainty in temperature is then determined over a typical range of nominal test surface temperatures. The results are displayed in figure 11. Assuming that in the ideal case of perfect heat transfer and no cooling, all objects in the measurement setup will have the maximum temperature, this range corresponds to a temperature ratio range of $\Gamma \approx 1 \ldots 1.6$.

The error is shown for an area where the offset radiance is at its maximum value (upper half) and for an area where a low offset radiance is present (lower half). For high surface temperatures, the share of offset radiation compared to the total radiation is low. Thus, the effect of the correction method is low for this case. The lower the surface temperatures, however, the greater the effect of the new correction method. At a common value of the test surface temperature of $T_{\text{surf}} = 350$ K, the relative error is reduced from approximately 8% to approximately 2% by using the correction method presented in this study. This shows the importance of considering the radiation situation in a test setup for the determination of high-quality results.

7. Conclusion

This paper has demonstrated the importance of considering a spatially resolved calibration procedure for high accuracy infrared thermography. Especially when facing adverse measurement conditions with disadvantageous temperature and thus radiation ratios between the object of interest and its surroundings, a spatially resolved corrections must be applied.

Consequently, a procedure to correct the offset radiance, which is the main source of measurement uncertainty when following the proven approach developed by Ochs *et al* [13, 18] in the recent past, was presented. Using a two-step procedure by calculating a non-dimensional, spatially resolved correction factor and subsequently applying this correction to a physical calibration makes the new procedure robust and simple to conduct.

The feasibility of this approach was shown by using a proven test rig for thermal measurements at the Institute of Thermal Turbomachinery (ITS). The corrected results are in excellent agreement with correlations and also with the expected results considering the well-known boundary conditions.

Additionally, an error estimation was performed. The linear propagation computation does show a large reduction in measurement uncertainty which is in good agreement with the presented experimental results. The estimation clearly shows that especially with increasing temperature ratios Γ, the additional effort for the proposed correction is well justified.

This procedure can be applied to almost every setup using infrared thermography to determine surface temperatures. Care has to be taken when surfaces with strongly concave features are present. An intersection of rays with the surface itself then has to be considered. This may be achieved by adding the test surface (usually with a coarser discretization) to the ray-triangle-intersection problem and adding the surface parameters ε_{ts}, T_{ts}. The following calibration steps can be performed as presented, yielding a comparable reduction in measurement uncertainty.

ORCID iDs

Maximilian Elfner https://orcid.org/0000-0002-3635-5175

References

[1] Lorenz M *et al* 2013 A novel measuring technique utilizing temperature sensitive paint—measurement procedure, validation, application, and comparison with infrared thermography *J. Turbomach.* **135** 031003
[2] Brack S, Poser R and von Wolfersdorf J 2016 A comparison between transient heat transfer measurements using TLC and IR thermography *Biennial Symp. on Measuring Techniques in Turbomachinery* p 9
[3] Axtmann M *et al* 2016 Endwall heat transfer and pressure loss measurements in staggered arrays of adiabatic pin fins *Appl. Therm. Eng.* **103** 1048–56
[4] Nathan M L *et al* 2014 Adiabatic and overall effectiveness for the showerhead film cooling of a turbine vane *J. Turbomach.* **136** 1537–47
[5] Kneer J *et al* 2015 A new test facility to investigate film cooling on a non-axisymetric contoured turbine endwall, part II: heat transfer and film cooling measurements *Proc. ASME Turbo Expo* pp GT2015–42524
[6] Stimpson C K, Snyder J C and Thole K A 2018 Effects of coolant feed direction on additively manufactured film cooling holes *Proc. ASME Turbo Expo* pp GT2018–77287
[7] Fraas M *et al* 2019 Optimized inlet geometry of a laidback fan-shaped film cooling hole—experimental study of film cooling performance *Int. J. Heat Mass Transfer* **128** 980–90

[8] Lohrengel J and Todtenhaupt R 1996 Wärmeleitfähigkeit, gesamtemissionsgrade und spektrale emissionsgrade der beschichtung nextel velvet coating 811–21 *PTB-Mitt.* **106** 259–65
[9] Brandt R, Bird C and Neuer G 2008 Emissivity reference paints for high temperature applications *Elsevier Meas.* **41** 731–6
[10] Dury M R *et al* 2007 Common black coatings—reflectance and ageing characteristics in the 0.32–14.3 μm wavelength range *Opt. Commun.* **270** 262–72
[11] Ianiro A and Cardone G 2010 Measurement of surface temperature and emissivity with stereo dual-wavelength IR thermography *J. Mod. Opt.* **57** 1708–15
[12] Hijazi A *et al* 2011 A calibrated dual-wavelength infrared thermometry approach with non-greybody compensation for machining temperature measurements *Meas. Sci. Technol.* **22** 025106
[13] Ochs M *et al* 2009 A novel calibration method for an infrared thermography system applied to heat transfer experiments *Meas. Sci. Technol.* **20** 075103
[14] Martiny M *et al* 1996 *In situ* calibration for quantitative infrared thermography *Qirt Eurotherm Series 50* vol 96 (https://doi.org/10.21611/qirt.1996.001)
[15] Schulz A 2000 Infrared thermography as applied to film cooling of gas turbine components *Meas. Sci. Technol.* **11** 948
[16] Bogard D G and Albert J E 2013 Measurements of adiabatic film and overall cooling effectiveness on a turbine vane pressure side with a trench *J. Turbomach.* **135** 051008
[17] Kirollos B and Povey T 2016 Laboratory infra-red thermal assessment of laser-sintered high_pressure nozzle guide vanes to De-Risk engine design programmes *Proc. ASME Turbo Expo* pp GT2016–57382
[18] Ochs M, Schulz A and Bauer H-J 2010 High dynamic range infrared thermography by pixelwise radiometric self calibration *Infrared Phys. Technol.* **53** 112–9
[19] Sakuma F and Kobayashi M 1996 Interpolation equations of scales of radiation thermometers *Proc. TEMPMEKO* pp 305–10
[20] Saunders P 1997 General interpolation equations for the calibration of radiation thermometers *Metrologia* **34** 201–10
[21] Saunders P and White D R 2003 Physical basis of interpolation equations for radiation thermometry *Metrologia* **40** 195–203
[22] Gubareff G G *et al* 1960 *Thermal Radiation Properties Survey: a Review of the Literature* (Minneapolis, MN: Minneapolis-Honeywell Regulator Company) p 293
[23] Teller S J 1992 Computing the antipenumbra of an area light source *Proc. 19th Annual Conf. on Computer Graphics and Interactive Techniques* vol 26 (https://doi.org/10.1145/133994.134029)
[24] Amanatides J and Choi K 1995 Ray tracing triangular meshes *Proc. Eighth Western Computer Graphics Symp.*
[25] Thomas M, Joseph R and Tropf W 1988 Infrared transmission properties of Sapphire, Spinel, Yttria, and ALON as a function of temperature and frequency *Appl. Opt.* **27** 239–45
[26] Fowles G R 1989 *Introduction to Modern Optics* 2nd edn (New York: Dover)
[27] Glasenapp T *et al* 2017 A new test rig for the investigation of film cooling on rough surfaces *Proc. 17th Int. Symp. on Transport Phenomena and Dynamics of Rotating Machinery*
[28] Reynolds W C, Kays W M and Kline S J 1958 Heat transfer in the turbulent incompressible boundary layer. Part 2: step wall-temperature distribution *NASA Memorandum* **12**
[29] Ochs M 2011 Filmkühlung transsonischer Turbinen: Infrarotthermographisches Messverfahren zur Charakterisierung des Wärmeübergangs *Dissertation* Karlsruhe Institute of Technology
[30] Elfner M 2019 *Bewertung Neuer Verfahren zur Kühlung von Turbinenrotorschaufeln Dissertation* Karlsruhe Institute of Technology p 140
[31] Flir 2019 *FLIR SC600 Manual* (http://dmintrade.com/wp-content/themes/twentyten/pdf/SC6000%20MWIR%206000%20Series%20Datasheetpdf.pdf)